JOURNAL OF SOLID STATE CHEMISTRY **141,** 17–28 (1998)
ARTICLE NO. SC987889

New Layered Compounds through Polysulfide Flux Synthesis; $A_2Sn_4S_9$ (A = K, Rb, Cs) Present a New Form of the $[Sn_4S_9]^{2-}$ Network

Gregory A. Marking,* M. Evain,† V. Petricek,‡ and Mercouri G. Kanatzidis*,[1]

*Department of Chemistry and the Center for Fundamental Materials Research, Michigan State University, East Lansing, Michigan 48824; †I.M.N., UMR CNRS C6502, Université de Nantes, Laboratoire de Chimie des Solides, 2 rue de la Houssinière, BP 32229, 44322 Nantes Cedex 03, France; and ‡Institute of Physics, Academy of Sciences of the Czech Republic, Na Slovance 2, 180 40 Praha 8, Czech Republic

Received December 24, 1997; revised May 11, 1998; accepted May 16, 1998

Crystals of $Cs_2Sn_4S_9$, $Rb_2Sn_4S_9$, and $K_2Sn_4S_9$ were synthesized by reacting Sn with Cs_2S_x, Rb_2S_x, or K_2S_x fluxes at 500°C. They can also be prepared as microcrystalline products through direct combination reactions at temperatures ranging from 720 to 750°C. The new ternary sulfide $Cs_2Sn_4S_9$ crystallizes in the orthorhombic *Pnma* space group, the new ternary sulfide $Rb_2Sn_4S_9$ crystallizes in the orthorhombic $P2_12_12_1$ space group, and the new ternary sulfide $K_2Sn_4S_9$ appears to be isostructural with $Rb_2Sn_4S_9$, as determined through X-ray powder diffraction. The structures of $Cs_2Sn_4S_9$, $Rb_2Sn_4S_9$, and $K_2Sn_4S_9$ consist of nearly identical $[Sn_4S_9]^{2-}$ layers which are stacked in two different arrangements. Alkali metal Cs^+, Rb^+, and K^+ cations are located between the layers. Raman and far-IR spectroscopic data confirm the presence of the $[Sn_4S_9]^{2-}$ layer in all three compounds. Single crystal optical spectra indicate that $Cs_2Sn_4S_9$, $Rb_2Sn_4S_9$, and $K_2Sn_4S_9$ are wide band-gap semiconductors with bandgaps of 2.66 eV, 2.65 eV, and 2.66 eV, respectively. © 1998 Academic Press

INTRODUCTION

The chemistry of multinary tin chalcogenides has been extensively investigated in the past and is a topic of much interest today as well. Many alkali and alkaline earth ternary tin chalcogenides such as Ba_2SnS_4 (1), $Na_6Sn_2S_7$ (2), and A_2SnS_3 (3), have been prepared through traditional solid state techniques. More recently, multinary tin sulfides and selenides have been synthesized through solvothermal syntheses with the goal of producing commercially applicable microporous chalcogenides (4, 5). Open framework compounds such as $Cs_2Sn_3Se_7$ (6), $[enH_2][Sn_3S_7]\cdot\frac{1}{2}en$ (7), $[NMe_4]_2\cdot Sn_3S_7\cdot H_2O$, (8), TEA-SnS-1 (9), and $Cs_4Sn_5S_{12}$ (10), formed through solvothermal techniques, have related structures based upon large interconnected rings with a shortest size of 24 atoms. It is interesting to note that the analogous compound $Rb_2Sn_3S_7\cdot 2H_2O$ (10) is also formed through solvothermal synthesis but has a completely different structure which is based upon a much smaller 8-member ring and chains of condensed SnS_6 octahedra. A growing number of similar open-framework structures based on $Sn_4S_9^{2-}$ anionic layers have also been reported (12, 13). Also in recent years, ternary alkali metal tin chalcogenides including $K_2Sn_2S_8$, α- and β-$Rb_2Sn_2S_8$, $Cs_2Sn_2S_6$, Cs_2SnS_{14} (14), $Cs_2Sn_3S_7\cdot\frac{1}{2}S_8$ (15) have been prepared through the molten alkali metal polychalcogenide flux technique of synthesis (16).

During exploratory investigations on the reactivity of tin in molten alkali polychalcogenides, some results of which have already been published in detail (14, 15), we discovered a series of unusual compounds with a new type of open tin-sulfide layered framework. We report here the flux synthesis and characterization of $Cs_2Sn_4S_9$, $Rb_2Sn_4S_9$, and $K_2Sn_4S_9$, a new group of alkali metal tin sulfides which contain a previously unknown type of $[Sn_4S_9]^{2-}$ layer (12, 13).

EXPERIMENTAL SECTION

Synthesis

All manipulations were carried out under a nitrogen atmosphere. Reagents were used as obtained: (i) Sn metal, 99.8%, −325 mesh, Cerac, Milwaukee, WI; (ii) sulfur powder, sublimed, Mallinckrodt, Paris, KY; (iii) cesium metal, 99.98%, Cerac, Milwaukee, WI; (iv) rubidium metal, 99.8%, Cerac, Milwaukee, WI; (v) potassium metal, analytical reagent, Mallinckrodt, Paris, KY. Cs_2S, Rb_2S, and K_2S were prepared using a modified literature procedure as reported previously (14).

Thin plates of $Cs_2Sn_4S_9$, $Rb_2Sn_4S_9$, and $K_2Sn_4S_9$ can be prepared through sulfur-rich polychalcogenide flux reactions kept for four days at 500°C and then cooled to 200°C at −4°C/h. All three compounds were also prepared in high

[1]Corresponding author.

0022-4596/98 $25.00

yield through direct combination reactions after differential thermal analyses (DTA) indicated that these materials melt and recrystallize congruently. Gold flaky plates of $Cs_2Sn_4S_9$ can be prepared as the major phase and isolated in an estimated 80% yield by reacting a mixture of $Cs_2S + 2Sn + 12S$ at 500°C. Greenish-yellow chunks of $Cs_2Sn_3S_7^1 \cdot \frac{1}{2}S_8$ (14) form as a minor phase. $Cs_2Sn_4S_9$ can also be prepared as a pure microcrystalline phase and isolated in 83% yield (based on Sn) by direct combination of $Cs_2S + 4Sn + 8S$ at 720°C for one day. Yellow-gold flaky plates of $Rb_2Sn_4S_9$ were prepared as the major phase (estimated as 80% of the isolated product) by reacting a mixture of $Rb_2S + 4Sn + 16S$ at 500°C. Small amounts of brown microcrystalline SnS_2 also result and were characterized only through SEM-EDS (scanning electron microscopy-energy dispersive spectroscopy). The use of less tin in similar flux reactions resulted in the formation of flat orange needles of β-$Rb_2Sn_2S_8$ (14) as the major phase. Direct combination of $Rb_2S + 4Sn + 8S$ at 750°C for three days results in nearly pure microcrystalline $Rb_2Sn_4S_9$ with an 89% yield (based on Sn) after isolation. Thin poor quality yellowish-gold "mica-like" crystals of $K_2Sn_4S_9$ were prepared as the major phase with an estimated 40% yield after isolation by reacting $K_2S + 3Sn + 12S$ at 500°C. Bright yellow chunks of $K_2Sn_2S_5$ (14) and brown flakes of SnS_2 are formed as minor phases. Direct combination with a slight excess of K_2S_4 flux at 750°C for three days resulted in nearly pure microcrystalline $K_2Sn_4S_9$ in 48% yield (based on Sn) after isolation.

Products from the flux and direct combination reactions were washed with DMF to remove excess alkali metal polysulfide flux and other soluble byproducts. A brief wash with H_2O removed small amounts of water-soluble phases from the products. Acetone and diethyl ether were used to rinse and dry the products. All three $A_2Sn_4S_9$ (A = K, Rb, Cs) compounds are stable in water and other common solvents and no decomposition can be detected in samples left under ambient atmospheric conditions for extended periods of time (at least two years).

Powder X-ray diffraction patterns were obtained from the pure yellow-gold flakes after small amounts of impurity phases were manually removed from the samples. Comparison of the calculated and experimental X-ray powder diffraction patterns confirmed the phase purity of all three samples. Semiquantitative analyses were performed on at least three different crystals of these phases, using SEM-EDS, and showed their compositions to be $Cs_{1.5}Sn_{4.0}S_9$, $Rb_{1.9}Sn_{3.9}S_9$, and $K_{1.7}Sn_{4.0}S_9$ which are close to the stoichiometries refined for the Cs and Rb compounds and postulated for the K analog.

Physical Measurements

Raman spectra were recorded using a BIO-RAD FT Raman Spectrometer with a Spectra-Physics Topaz T10-106c laser. FT-IR spectra for this compound were recorded as solids in a CsI matrix. Data were recorded from the far-IR region (650–100 cm^{-1}, 4 cm^{-1} resolution) with the use of a Nicolet 740 FT-IR spectrometer equipped with a TGS/PE detector and beam splitter. Semiquantitative microprobe analysis were performed with a JEOL JSM-6400V scanning electron microscope (SEM) equipped with a Tracor Northern energy dispersive spectroscope (EDS) detector. Data acquisitions were performed using an accelerating voltage of 20 kV and a 30-s accumulation time. Powder X-ray diffraction (XRD) was performed using a calibrated Phillips XRD-3000 controlled by a PDP 11 computer using Ni-filtered Cu radiation and operating at 40 kV and 20 mA. Guinier film techniques were also used to obtain powder X-ray diffraction results. Calculated X-ray powder patterns used for comparative purposes were obtained using Cerius^2 software (17).

Optical transmission measurements were made at room temperature on single crystals using a Hitachi U-6000 microscopic FT spectrophotometer with an Olympus BH-2 metallurgical microscope over a range from 380–900 nm.

Differential thermal analyses (DTA) were performed using a computer-controlled Shimadzu DTA-50 thermal analyzer. Approximate 20-mg amounts of sample were sealed in quartz tubes under vacuum and then heated at 10°C/min to 700°C or 750°C isothermed from 10 min and finally cooled to 100°C or 200°C at 10°C/min. Empty sealed quartz tubes of approximately the same mass as the sample tubes were present on the reference side of the detector during measurements. The DTA samples were examined by powder X-ray diffraction after the experiments.

X-Ray Crystallography

A single crystal of $Cs_2Sn_4S_9$ with a thin plate-like shape was mounted on a glass fiber and an intensity data set was collected using a Rigaku AFC6S diffractometer with graphite monochromated Mo Kα radiation operating at 50 kV and 30 mA at room temperature. Three standard reflections were monitored every 300 reflections and indicated that no significant decay occurred. Unique data (h, k, l) were collected out to 50° in 2θ using ω-2θ scans. The diffraction data were processed and the structure was refined using TEXSAN software (18). The initial structural model was found using direct methods (SHELXS-86) (19) and the disordered Cs^+ cationic positions were found through the difference Fourier technique.

The data were corrected for Lorentz and polarization effects, an empirical absorption correction based on ψ-scans was applied to the data, and equivalent data were averaged. The structural model quickly converged to R/R_w of 4.7%/6.3% but one Cs^+ cation was found to be extremely cylindrical in shape. When this Cs^+ position was split into

two positions, their thermal parameters became less extreme but the R/R_w showed no improvement. An additional electron density peak indicated that the cesium cation was further disordered. The refinement did not converge well when the occupancies and anisotropic thermal parameters of the disordered Cs^+ positions were refined simultaneously. The occupancies of the disordered Cs^+ atoms were first held constant while the thermal and all other parameters were refined and then the disordered Cs^+ atom thermal parameters were held constant while the disordered site occupancies and all other parameters were refined. This cycle was repeated until the refinement results became consistent. After complete anisotropic refinement with the cesium cation disordered over three positions, the R and R_w were 3.9% and 5.0%, respectively.

A thin plate-like crystal of $Rb_2Sn_4S_9$ was also mounted on a glass fiber and an intensity data set was collected using a Rigaku AFC6S diffractometer with graphite monochromated Mo Ka radiation operating at 50 kV and 30 mA at room temperature. Three standard reflections were monitored every 300 reflections and indicated no significant decay. Unique data from the *hkl* octant were collected out to 50° in 2θ using ω scans. The diffraction data were processed and refined using the TEXSAN software (18) and the structural model was found using SHELXS-86 (19) direct methods. Although the data had no apparent errors and the structure made complete chemical sense, the refinement was not satisfactory with a best R and R_w of 16% and 18%. The unit cell parameters and bond distances had large esd's and were also unsatisfactory. These poor results were due presumably to twinning.

A sample of $Rb_2Sn_4S_9$ and the results of the unsatisfactory refinement discussed above were sent to the Université de Nantes in France for data collection and further structural refinement. A flat plate crystal was first tested on a Weissenberg camera and preliminary lattice parameters were obtained. The crystal was glued to the tip a of Lindemann capillary and data were collected using an Enraf–Nonius CAD-4F diffractometer for high $\sin(\theta)/\lambda$ reflections and a Stoe IPDS diffractometer was used to measure weak intensities at low $\sin(\theta)/\lambda$ values in a high resolution mode.

Data reduction, absorption correction, and all refinements were carried out with the JANA96 program package (20). The measured intensities were corrected for scale variation based upon standards (CAD4 data set only) and Lorentz and polarization effects (CAD4 and IPDS sets). A Gaussian-type analytical absorption correction was applied and both data sets were merged on a common scale established from mutual intense reflections. The final solution model proved to be nearly identical to that from the unsatisfactory refinement discussed above, using the orthorhombic space group $P2_12_12_1$ and a structural model related to that of $Cs_2Sn_4S_9$. A vast improvement in the refinement results was obtained because high precision data collection and the JANA96 (20) software enabled detection and refinement of a contact twinned crystal with the following merohedral rotation twinning matrix:

$$M = \begin{pmatrix} 0 & 1 & 0 \\ 1 & 0 & 0 \\ 0 & 0 & -1 \end{pmatrix}.$$

The model proved correct with an unweighted R value smoothly converging to 4.8% and a volume ratio for the two orientations close to 1:1. A large thermal parameter was calculated for one of the rubidium atoms (Rb4), suggesting a distribution of rubidium atoms in between the $[Sn_4S_9]^{2-}$ layers much like the disordered Cs^+ in $Cs_2Sn_4S_9$. A splitting of the original Rb4 position slightly improved the modeling of the electron density, the residual unweighted R value being brought down to 4.6%. Table 1

TABLE 1
Crystal Data for $Cs_2Sn_4S_9$ and $Rb_2Sn_4S_9$

Formula	$Cs_2Sn_4S_9$	$Rb_2Sn_4S_9$
fw	1029.11	934.3
a, Å	13.401(4)	11.8910(7)
b, Å	11.973(2)	11.8867(11)
c, Å	12.034(2)	25.915(2)
Z, V (Å^3)	4, 1930.8(1.4)	8, 3662.9(8)
Space group	Pnma #62	$P2_12_12_1$ #19
d_{calc} (g/cm^3)	3.540	3.387
Crystal size, mm^3	$0.34 \times 0.23 \times 0.04$	$0.10 \times 0.11 \times 0.02$
Temp (°C)	23	20
Radiation	Mo Kα	Mo Kα
μ (Mo Kα), cm^{-1}	97.45	115.0
Scan mode	2θ-ω	2θ-ω/ω
Scan speed, °/min	4	NA
2θ max, deg	50	60
# data collected	1968	21,874
# unique data	1968	10363
# data observed, $I > 3\sigma(I)$	1116	5187
# variables	94	282
Absorption correction	ψ-scans	Analytical
Abs. ratio (min/max)	0.3961	0.2297
R/R_w[b], %	3.9/5.0	4.6/5.0
GOF	1.72	1.33
Residual e-density (pos/neg)	+1.616/−1.087	+2.8/−1.5
Twin matrices for $Rb_2Sn_4S_9$,	$\begin{pmatrix} 1 & 0 & 0 \\ 0 & 1 & 0 \\ 0 & 0 & 1 \end{pmatrix}$,	$\begin{pmatrix} 0 & 1 & 0 \\ 1 & 0 & 0 \\ 0 & 0 & -1 \end{pmatrix}$
Twin fractions for $Rb_2Sn_4S_9$ (%)	53.79(6),	46.21

[b] $R = \sum(|F_o| - |F_c|)/\sum|F_o|$, $R_w = \{\sum_w(|F_o| - |F_c|)^2/\sum_w|F_o|^2\}^{1/2}$.

TABLE 2
Positional Parameters for $Cs_2Sn_4S_9$

Atom	*x*	*y*	*z*
$Cs_2Sn_4S_9$			
Cs1	0.4395(1)	1/4	0.0783(1)
Cs2	0.537(2)	0.226(2)	0.546(2)
Cs2′	0.545(4)	0.317(6)	0.538(4)
Cs2″	0.281(2)	1/4	0.887(2)
Sn1	0.72817(8)	0.39959(9)	0.18360(8)
Sn2	0.6786(1)	0.4121(1)	0.87535(8)
S1	0.6578(1)	1/4	0.2948(4)
S2	0.2901(5)	1/4	0.4526(4)
S3	0.5814(5)	1/4	0.8286(4)
S4	0.8450(3)	0.4500(4)	0.8249(3)
S5	0.8939(3)	0.4663(4)	0.2299(3)
S6	0.6199(3)	0.4896(3)	0.0486(3)

Note. Cs2 is 64% occupied, Cs2′ is 28% occupied, and Cs2″ is 8% occupied.

contains pertinent crystallographic data for $Cs_2Sn_4S_9$ and $Rb_2Sn_4S_9$, while Tables 2 and 3 contain atomic parameters, and Tables 4 and 5 contain anisotropic thermal parameters for these two compounds.

RESULTS AND DISCUSSION

Structure

Although not isomorphous, $Cs_2Sn_4S_9$ and $Rb_2Sn_4S_9$ have the same infinite two-dimensional framework, consisting of corrugated anionic $[Sn_4S_9]^{2-}$ layers with alkali metal cations located between the layers. The basic building block of these layers is the Sn_4S_9 cluster (see Scheme 1) which is composed of two tetrahedral SnS_4 and two trigonal pyramidal SnS_3 units fused into the larger unit through edge- or corner-sharing of sulfur atoms. These Sn_4S_9 clusters associate into layers by coordinating to each other via intercluster Sn-S bonds. Each Sn_4S_9 fragment is connected to four others in a nearly face-centered arrangement through $(\mu\text{-S})_2$ bridges forming the overall $[Sn_4S_9]^{2-}$ layer found in both compounds. The intercluster Sn-S bonds give rise to the observed five-coordinate as well as tetrahedral tin centers in the layer (see dotted lines in Scheme 1).

The Sn_4S_{13} cluster, shown in Fig. 1, represents an excised group from the layered structure and includes the basic Sn_4S_9 cluster plus several sulfur atoms from neighboring clusters. In this group one can see two types of subfragments, namely Sn_2S_8 and Sn_2S_7. The Sn_2S_8 fragment is highlighted in Scheme 1. The latter is formed by the corner-sharing of two SnS_4 tetrahedra. There are also short contacts between the apical sulfur of the Sn_2S_8 fragment and the tin atoms of the Sn_2S_7 fragment: 2.859(6) Å and 3.381(6) Å in $Rb_2Sn_4S_9$ and 3.279(4) Å in $Cs_2Sn_4S_9$. The layers have relatively large open areas which can be seen in a view perpendicular to the $[Sn_4S_9]^{2-}$ layer in $Cs_2Sn_4S_9$ (Fig. 2A). The corresponding layer in $Rb_2Sn_4S_9$ is distorted relative to the one in the Cs analog and it shown in Fig. 2B.

TABLE 3
Atomic Positional Parameters for $Rb_2Sn_4S_9$

	x	*y*	*z*
Sn1	0.7053(1)	0.4606(1)	0.13901(7)
Sn2	0.1820(1)	0.9589(1)	0.11008(7)
Sn3	0.2033(1)	0.6600(1)	0.10764(6)
Sn4	0.3937(1)	0.4632(1)	0.15614(7)
Sn5	0.3699(1)	0.1432(1)	0.16426(7)
Sn6	0.8974(1)	0.6559(1)	0.09169(7)
Sn7	0.6854(1)	0.1656(1)	0.13806(6)
Sn8	0.8704(1)	0.9785(1)	0.08444(6)
Rb1	0.5523(2)	0.7004(2)	0.0408(1)
Rb2	0.4237(2)	0.8077(2)	0.2182(1)
Rb3	0.4779(3)	0.1946(3)	0.9818(1)
Rb4′	0.959(1)	0.886(1)	0.2700(3)
Rb4″	0.952(2)	0.783(6)	0.2674(6)
S1	0.0526(4)	0.8016(5)	0.1427(2)
S2	0.5544(5)	0.3190(5)	0.1043(2)
S3	0.8165(4)	0.8090(5)	0.0428(2)
S4	0.5488(5)	0.0655(5)	0.1889(3)
S5	0.7648(5)	0.5105(5)	0.0547(2)
S6	0.2270(5)	0.0180(6)	0.1980(3)
S7	0.8436(6)	0.6088(5)	0.1763(3)
S8	0.3112(5)	0.1240(5)	0.0782(3)
S9	0.5596(5)	0.5538(5)	0.1892(3)
S10	0.3116(5)	0.8201(6)	0.0773(2)
S11	0.0625(5)	0.5818(5)	0.0506(2)
S12	0.3299(4)	0.3120(5)	0.2109(2)
S13	0.7905(4)	0.3054(5)	0.1849(3)
S14	0.0471(5)	0.0385(5)	0.0502(3)
S15	0.2478(5)	0.5930(6)	0.1934(3)
S16	0.3404(5)	0.5105(5)	0.0705(2)
S17	0.8263(6)	0.0113(6)	0.1711(3)
S18	0.7394(5)	0.1170(6)	0.0506(3)

Note. Rb4′ is 62(3)% occupied and Rb4″ is 38% occupied.

TABLE 4
Anisotropic Displacement Parameters for $Cs_2Sn_4S_9$

Atom	*U11*	*U22*	*U33*	*U12*	*U13*	*U23*
Cs1	0.040(1)	0.0214(8)	0.032(8)	0	0.0060(7)	0
Cs2	0.031(4)	0.07(6)	0.022(2)	0.005(8)	0.003(2)	0.01(1)
Cs2′	0.032(9)	0.06(3)	0.024(8)	−0.02(1)	0.013(6)	−0.03(1)
Cs2″	0.06(2)	0.03(1)	0.05(1)	−0.03(1)	−0.03(1)	0
Sn1	0.0291(6)	0.0188(5)	0.0183(5)	−0.0012(5)	−0.0041(5)	0.0018(5)
Sn2	0.0381(7)	0.0223(6)	0.0222(5)	−0.0063(6)	0.0080(5)	−0.0044(5)
S1	0.050(4)	0.020(3)	0.018(3)	0	0.013(3)	0
S2	0.034(4)	0.023(3)	0.018(3)	0	−0.003(3)	0
S3	0.036(4)	0.016(3)	0.026(3)	0	−0.012(3)	0
S4	0.034(3)	0.032(2)	0.033(2)	0.002(2)	0.004(2)	0.016(2)
S5	0.031(2)	0.027(2)	0.028(2)	0.000(2)	−0.001(2)	−0.003(2)
S6	0.037(2)	0.023(2)	0.018(2)	0.008(2)	−0.001(2)	−0.002(2)

The expression of the harmonic displacement factor is:

$$\exp\left(-2\pi^2 \sum_i \sum_j h_i a^i U^{ij} a^j h_j\right), \text{ with } U^{ij} \text{ in Å}$$

TABLE 5
Anisotropic Displacement Parameters for $Rb_2Sn_4S_9$, *U(i, j)* ($Å^2$)

Atom	*U11*	*U22*	*U33*	*U12*	*U13*	*U23*
Sn(1)	0.0187(8)	0.0190(8)	0.0263(9)	0.0031(6)	0.0058(7)	0.0042(7)
Sn(2)	0.0130(7)	0.0163(8)	0.025(1)	0.0010(6)	−0.0005(6)	−0.0029(7)
Sn(3)	0.0184(8)	0.0158(8)	0.0239(9)	−0.0011(6)	−0.0044(7)	0.0022(6)
Sn(4)	0.0203(8)	0.0195(8)	0.035(1)	−0.0050(6)	−0.0075(7)	0.0086(7)
Sn(5)	0.0197(8)	0.0135(7)	0.032(1)	0.0009(6)	−0.0039(7)	−0.0048(7)
Sn(6)	0.0199(8)	0.0225(9)	0.031(1)	0.0048(7)	0.0091(7)	0.0080(8)
Sn(7)	0.0154(7)	0.0139(8)	0.0241(8)	−0.0014(6)	0.0040(6)	−0.0026(6)
Sn(8)	0.0138(7)	0.0176(8)	0.031(1)	−0.0014(6)	0.0064(7)	−0.0064(7)
Rb(1)	0.021(1)	0.039(2)	0.049(2)	0.002(1)	−0.002(1)	0.005(1)
Rb(2)	0.028(1)	0.023(1)	0.045(1)	0.0000(9)	−0.000(1)	−0.003(1)
Rb(3)	0.057(2)	0.037(2)	0.049(2)	−0.005(1)	0.013(1)	0.003(2)
Rb(4)	0.044(5)	0.17(1)	0.048(5)	0.052(5)	−0.016(3)	−0.002(5)
Rb(4′)	0.041(8)	0.56(7)	0.047(8)	−0.12(2)	0.007(6)	−0.05(2)
Rb(4″)*	0.22					
S(1)	0.009(2)	0.013(3)	0.030(3)	0.000(2)	0.000(2)	−0.009(3)
S(2)	0.028(3)	0.015(3)	0.014(3)	0.012(2)	−0.010(2)	−0.009(2)
S(3)	0.016(3)	0.018(3)	0.030(3)	−0.002(2)	−0.003(2)	−0.001(3)
S(4)	0.012(3)	0.026(3)	0.047(4)	0.002(2)	0.003(3)	0.007(3)
S(5)	0.032(3)	0.014(3)	0.015(3)	−0.000(2)	0.002(3)	0.006(2)
S(6)	0.028(3)	0.041(4)	0.025(4)	−0.010(3)	−0.000(3)	−0.007(3)
S(7)	0.043(4)	0.022(3)	0.025(4)	−0.012(3)	0.007(3)	0.004(3)
S(8)	0.029(3)	0.021(3)	0.029(4)	−0.014(2)	0.001(3)	0.004(3)
S(9)	0.014(3)	0.022(3)	0.036(4)	0.005(2)	−0.005(3)	−0.012(3)
S(10)	0.020(3)	0.024(3)	0.043(4)	0.001(3)	0.014(3)	0.001(3)
S(11)	0.012(3)	0.027(3)	0.025(3)	0.007(2)	−0.005(2)	−0.008(3)
S(12)	0.024(3)	0.013(2)	0.026(3)	−0.003(2)	0.007(2)	0.001(3)
S(13)	0.013(3)	0.013(2)	0.054(4)	0.004(2)	−0.009(3)	0.001(3)
S(14)	0.015(3)	0.020(3)	0.047(4)	−0.001(2)	−0.003(3)	0.013(3)
S(15)	0.026(3)	0.023(3)	0.029(3)	0.003(2)	0.002(3)	0.008(3)
S(16)	0.021(3)	0.025(3)	0.020(3)	0.010(2)	−0.002(2)	−0.004(2)
S(17)	0.037(4)	0.039(4)	0.038(4)	0.016(3)	−0.007(3)	−0.001(3)
S(18)	0.032(4)	0.037(4)	0.022(3)	0.009(3)	−0.003(3)	−0.001(3)

*) isotropically refined.

The shortest S-S distance across the openings in this $[Sn_4S_9]^{2-}$ layer is 6.471(6) Å in $Cs_2Sn_4S_9$ and 6.073(6) Å in $Rb_2Sn_4S_9$.

In $Cs_2Sn_4S_9$, the layers are related to each other through an inversion center and are stacked so that the Sn_4S_{13} fragments and open areas alternate along the *a* axial direction forming cavities rather than channels. The shortest S-S interlayer contact in the cesium phase is 3.392(5) Å. There is no inversion center in $Rb_2Sn_4S_9$, but the layers stack in a similar fashion with the fragments and openings aligned along the *c* axial direction. The shortest S-S interlayer contact in the rubidium phase is 3.415(5) Å. The major difference between these two structures is that the layers are stacked two-by-two in $Rb_2Sn_4S_9$, leading to a doubled unit cell, relative to that of $Cs_2Sn_4S_9$. Figure 3 shows a projection down the *c* axis of the unit cell of $Cs_2Sn_4S_9$, parallel to the $[Sn_4S_9]^{2-}$ layers. In this view, it is apparent that the $[Sn_4S_9]^{2-}$ layers are aligned so that the corrugation, or modulation, is "in-phase" between layers. On the other hand, Fig. 4 shows a projection down the *b* axis of $Cs_2Sn_4S_9$, also parallel to the $[Sn_4S_9]^{2-}$ layers, which shows that the corrugations are "out-of-phase" between the layers in this direction. Channels are formed between the "out-of-phase" layers parallel to the *b* axis and the Cs^+ cations are disordered along these channels. The minimum sulfur-sulfur distance across these channels in $Cs_2Sn_4S_9$ is relatively large, 5.775 Å, and presumably this allows the Cs^+ cations some freedom of movement and accounts for the disordered occupancy of different cationic sites within the channel.

Figure 5 shows a projection down the *a* axis of the unit cell of $Rb_2Sn_4S_9$, parallel to the $[Sn_4S_9]^{2-}$ layer. In this structure, the layers are stacked in pairs. Along the *a* axis, the top two layers are "in-phase" with each other and the bottom two layers are also in phase with each other, but "out-of-phase" with the top two layers. Channels are formed between the two adjacent "out-of-phase" layers and Rb^+ cations (Rb3) are located in these channels. The shortest sulfur-sulfur distance across this channel is 4.624(7) Å and the Rb3 cations are not disordered. Figure 6 shows a projection down the *b* axis of the unit cell of $Rb_2Sn_4S_9$, parallel to the $[Sn_4S_9]^{2-}$ layer. In this case, along the *b* axis, the middle two layers are in phase with each other and the top and bottom layers are also in phase with each other, but out of

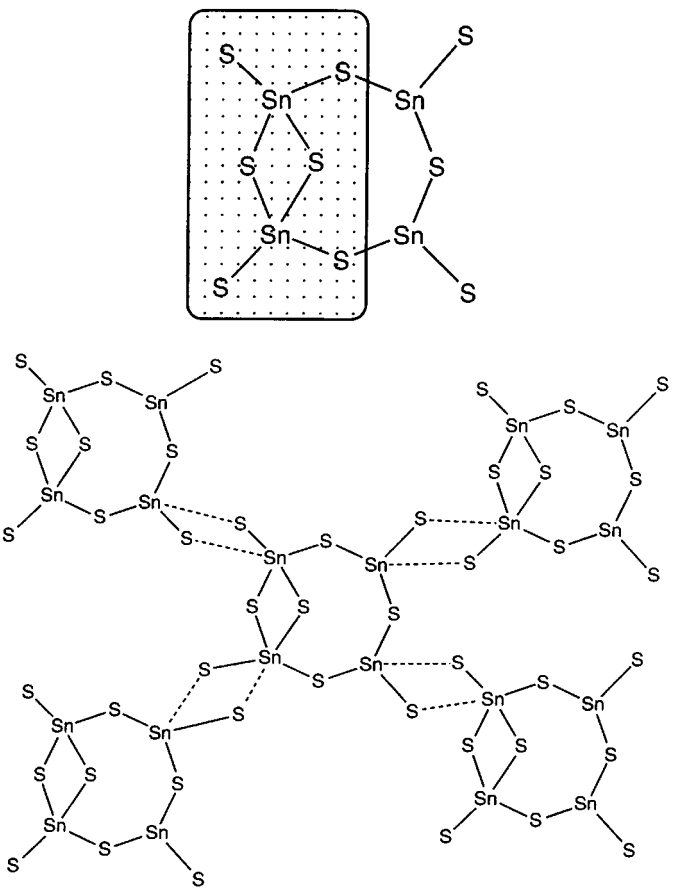

SCHEME 1

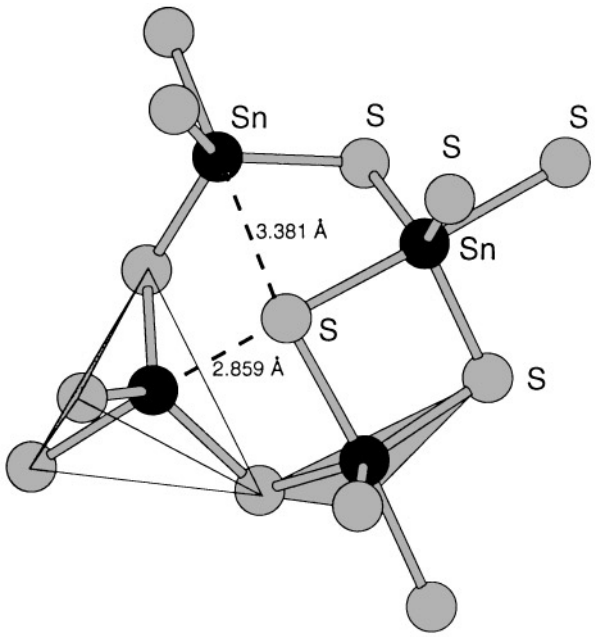

FIG. 1. A view of the Sn_4S_{13} fragment found in $A_2Sn_4S_9$ (A = K, Rb, and Cs). Note the tetrahedral and trigonal bipyramidal coordination of the Sn. The interatomic distances correspond to those found in $Rb_2Sn_4S_9$.

phase with the middle two layers. Channels are again formed between the two adjacent out of phase layers and Rb^+ cations (Rb4) are located in these channels. The minimum sulfur-sulfur distance across this channel is substantial, 5.696(8) Å, and the Rb4 cations are disordered in different positions along this channel in the same fashion that the Cs^+ cations are disordered in $Cs_2Sn_4S_9$. Tables 6, 7, and 8 contain selected interatomic distances and interatomic bond angles found in the Sn_4S_{13} units of $Cs_2Sn_4S_9$ and $Rb_2Sn_4S_9$.

It is interesting to contrast the previously reported $[Sn_4S_9]^{2-}$ layer (12, 13) (hereafter referred to as α-$[Sn_4S_9]^{2-}$) with the one described here. We note that the α-$[Sn_4S_9]^{2-}$ layer is stabilized with the large organic counterion Bu_4N^+. These two types of layers (i.e., α,β-$[Sn_4S_9]^{2-}$) are structural isomers and, other than the common chemical formula, they share very few structural features. First, α-$[Sn_4S_9]^{2-}$ is based on periodic arrays of Sn_3S_4 broken-cube clusters, while the one reported in this paper (β-$[Sn_4S_9]^{2-}$) is based on periodic arrays of Sn_4S_9 clusters. Second, the α-$[Sn_4S_9]^{2-}$ form contains very large rings while β-$[Sn_4S_9]^{2-}$ has considerably smaller rings. Third, in the former the Sn_3S_4 clusters are linked with SnS_4 tetrahedra, while in β-$[Sn_4S_9]^{2-}$ the layers are formed by direct association of Sn_4S_9 clusters. The stark contrast in the two structures underscores the great importance of the counterion effect (20). The counterion effect dictates that a reduction in dimensionality occur when the charge balancing counterions become sufficiently large (21). The large Bu_4N^+ cations favor a "stretched out" version of $[Sn_4S_9]^{2-}$ anion which requires large holes, while the small alkali

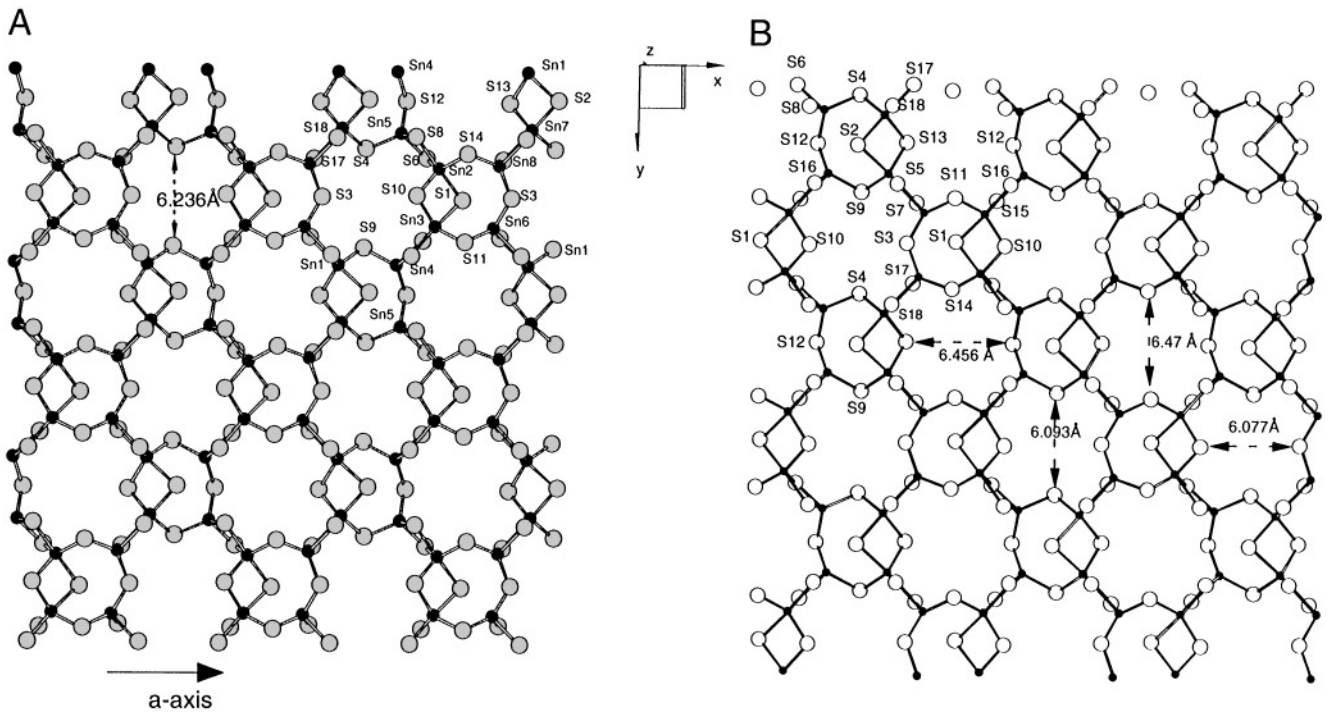

FIG. 2. The $[Sn_4S_9]^{2-}$ layer in $A_2Sn_4S_9$ (A = K, Rb, and Cs), viewed perpendicular to the layer. The sulfur-sulfur distance across the opening corresponds to that in $Cs_2Sn_4S_9$.

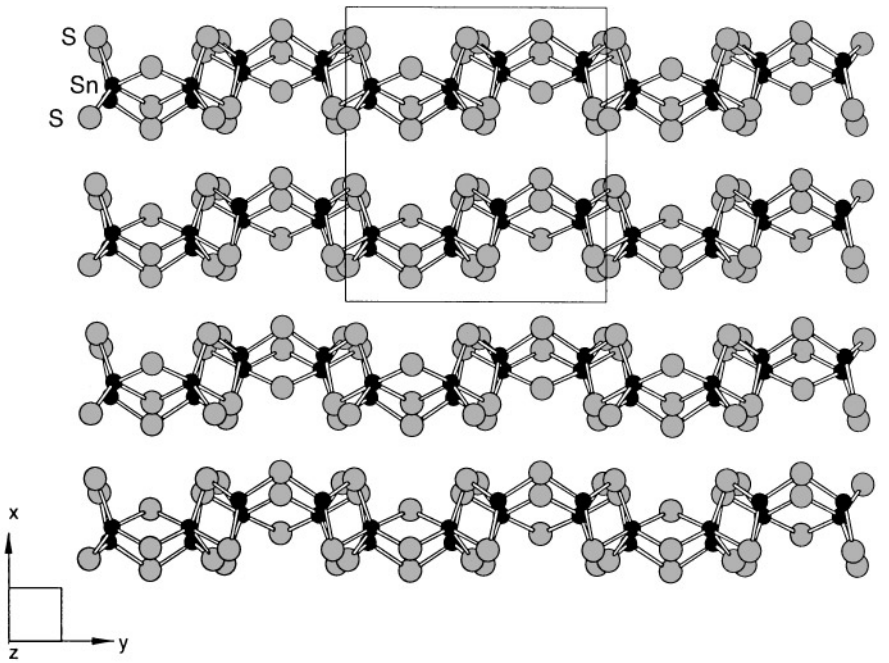

FIG. 3. A projection down the *c* axis of $Cs_2Sn_4S_9$, parallel to the $[Sn_4S_9]^{2-}$ layers, showing that the corrugated layers are in phase in this direction. The Cs atoms are omitted for clarity.

cations favor a contracted motif of the type we observed here. It is notworthy, however, that a counterion effect does not exist in going from K^+ to Rb^+ to Cs^+ as the structure of the anionic framework remains unchanged.

Apparently, the changes in alkali ion size are not sufficient in this case to cause a structural transition. It is not until the cation acquires a very large volume, as in Bu_4N^+, that a change towards lower connectivity in the $[Sn_4S_9]^{2-}$

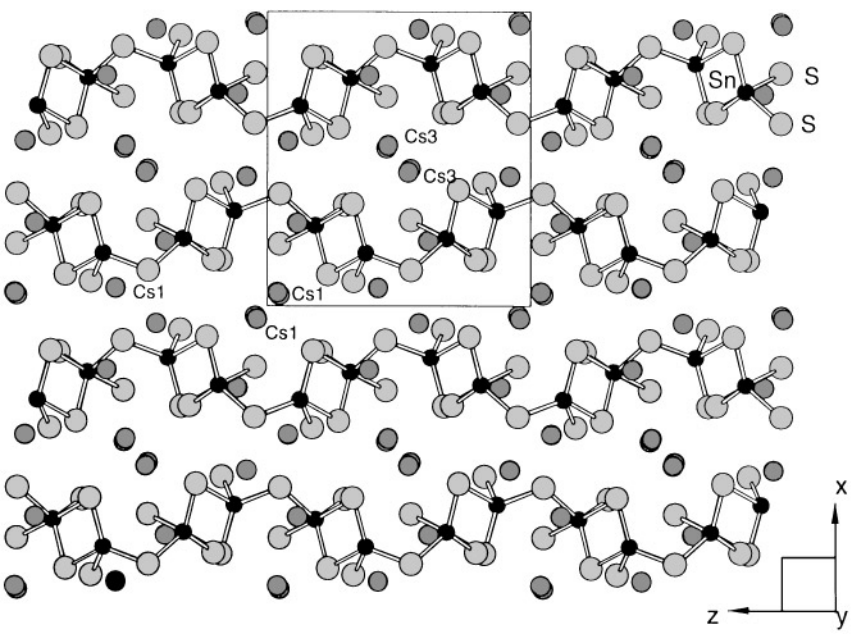

FIG. 4. A projection down the *b* axis of $Cs_2Sn_4S_9$, parallel to the $[Sn_4S_9]^{2-}$ layers, showing that the corrugated layers are out of phase in this direction. Note the Cs3 cations located in the channels formed by the out of phase corrugation in this direction.

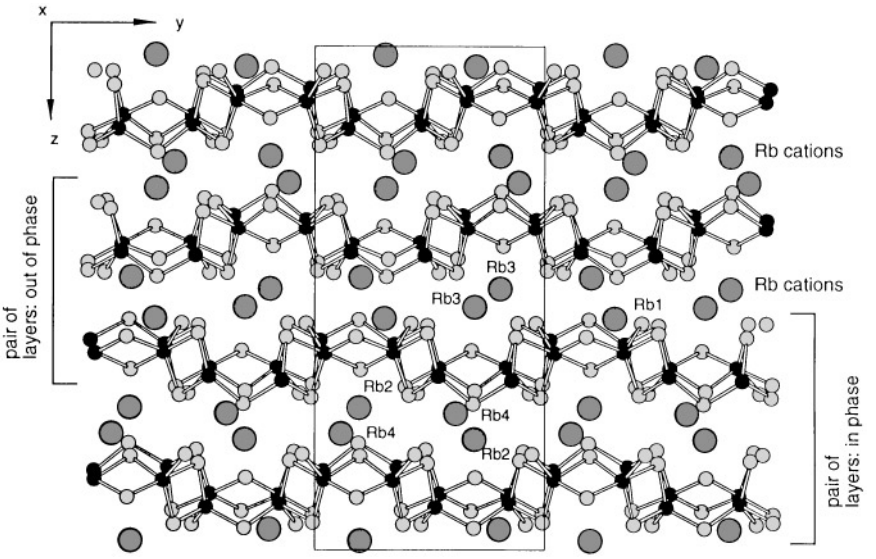

FIG. 5. A projection down the *a* axis of $Rb_2Sn_4S_9$, parallel to the $[Sn_4S_9]^{2-}$ layers, showing that the corrugated layers are stacked in pairs. The top two and bottom two layers are in phase with themselves but out of phase with each other in this direction. Note the Rb3 cations located in the small channels formed between out of phase layers.

framework is necessary. The lower connectivity (which is akin to lower dimensionality) (22) in the α-$[Sn_4S_9]^{2-}$ form is manifested via lower average coordination numbers for Sn and S, relative to that of the β-$[Sn_4S_9]^{2-}$ form. It is also noteworthy to point out that the disorder of the alkali atoms in $Cs_2Sn_4S_9$, $Rb_2Sn_4S_9$, and possibly in $K_2Sn_4S_9$ indicates that the available space between the layers is larger than the volume these cations can occupy (when fully packed). A consequence of this may be a good mobility of these ions in the interlayer spaces resulting in either high ionic conductivity or good ion-exchange properties.

Physical Measurements

Vibrational spectroscopies indicate that the structure and bonding characteristics of these three phases are closely

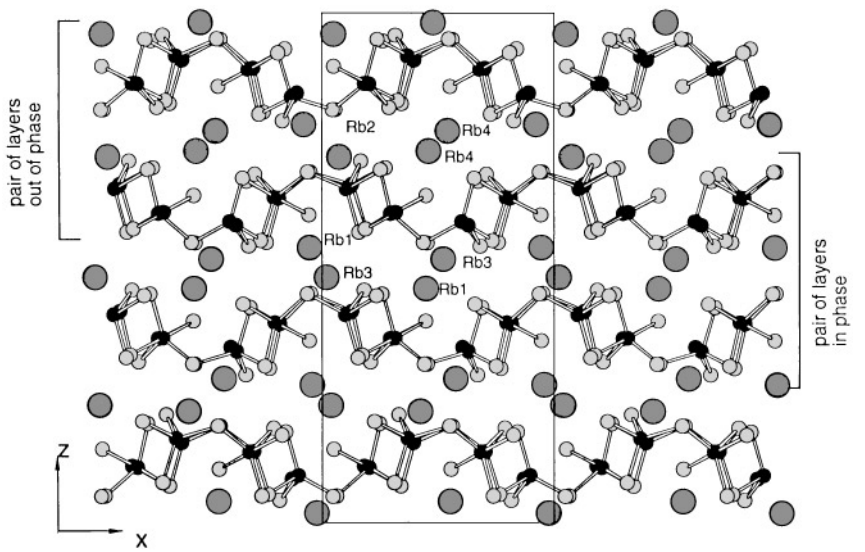

FIG. 6. A projection down the *b* axis of $Rb_2Sn_4S_9$, parallel to the $[Sn_4S_9]^{2-}$ layers, again showing that the corrugated layers are stacked in pairs. The middle two and top-bottom layers are in phase with themselves but out of phase with each other in this direction. Note the Rb4 cations located in the large channels formed between out of phase layers.

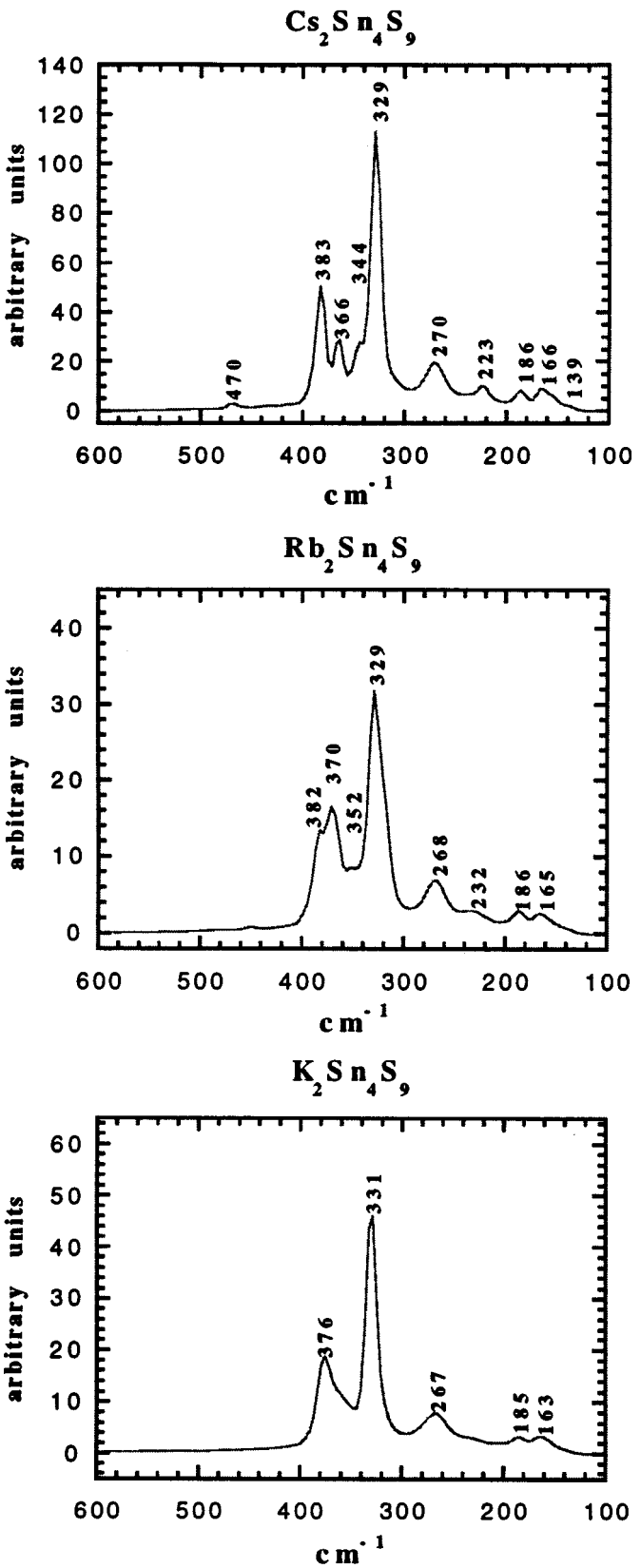

FIG. 7. Raman spectra from the region, 600–100 cm^{-1}, for (A) $Cs_2Sn_4S_9$, (B) $Rb_2Sn_4S_9$, and (C) $K_2Sn_4S_9$, at 4 cm^{-1} resolution.

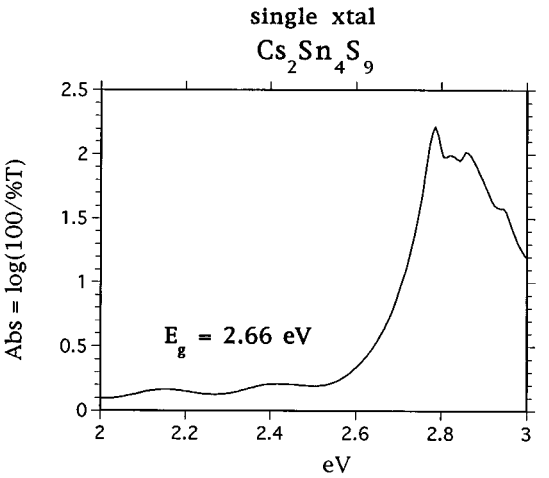

FIG. 8. Representative single crystal optical transmission spectrum collected from $Cs_2Sn_4S_9$ and converted to absorption data.

related. Similarities between the Raman spectra for $Cs_2Sn_4S_9$, $Rb_2Sn_4S_9$, and $K_2Sn_4S_9$ can be seen in Fig. 7. The Raman and far-IR absorptions for all three phases are listed in Table 9, and comparison of the various absorptions listed for each of the three phases in this table shows a nearly one-to-one correspondence. This correspondence strongly suggests that the $[Sn_4S_9]^{2-}$ layer, crystallographically determined to be present in both $Cs_2Sn_4S_9$ and $Rb_2Sn_4S_9$, is also present in $K_2Sn_4S_9$. It is likely that the $[Sn_4S_9]^{2-}$ layer in $K_2Sn_4S_9$ is slightly distorted, relative to the Cs and Rb analogs and the packing arrangement of the layers might be slightly different, but it is highly probable that the general form of the $[Sn_4S_9]^{2-}$ layer is the same for all three $A_2Sn_4S_9$ compounds. The absorption peaks between 400 cm^{-1} and 260 cm^{-1} in Fig. 7 and Table 9 are in the range of Sn-S vibrations. The absorptions below 260 cm^{-1} are harder to characterize. They may result from collective

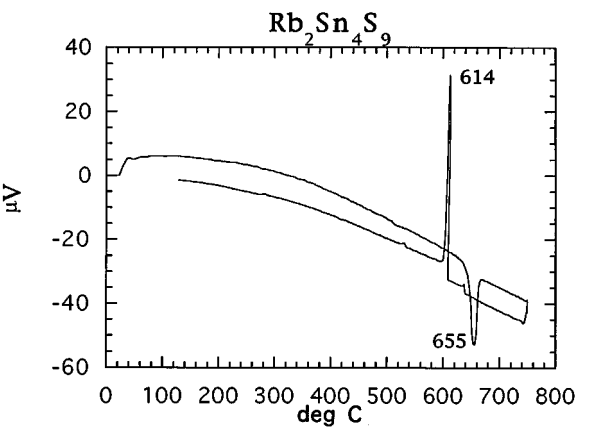

FIG. 9. Representative differential thermal analysis (DTA) data collected from $Rb_2Sn_4S_9$.

TABLE 6
Selected Interatomic Distances (Å) and Important Bond Angles (°) for $Cs_2Sn_4S_9$

Atoms	Distance	Atoms	Distance
avg Cs1–S	3.545(12) Å	avg Sn1–S	2.502 Å
avg Cs2–S	3.47(2) Å		
avg Cs3–S	3.49 (2) Å	Sn2–S3	2.404(4)
avg Cs4–S	3.54 (2) Å	Sn2–S4	2.356(5)
		Sn2–S5	2.475(4)
Sn1–S1	2.427(4) Å	Sn2–S6	2.414(4)
Sn1–S2	2.565(4) Å	avg Sn2–S	2.412
Sn1–S4	2.664(4) Å		
Sn1–S5	2.425(5) Å	Sn2–S2	3.208(5)
Sn1–S6	2.430(4) Å		
Atoms	**Angle (deg)**	**Atoms**	**Angle (deg)**
S1–Sn1–S2	87.9(1)	S3–Sn2–S4	127.5(2)
S1–Sn1–S4	90.2(1)	S3–Sn2–S5	95.6(2)
S1–Sn1–S5	118.2(2)	S3–Sn2–S6	107.2(2)
S1–Sn1–S6	117.7(2)	S4–Sn2–S5	94.3(1)
S2–Sn1–S4	177.1(2)	S4–Sn2–S6	117.2(2)
S2–Sn1–S5	94.6(2)	S5–Sn2–S6	104.9(1)
S2–Sn1–S6	94.3(2)		
S4–Sn1–S5	88.2(1)	Sn1–S1–Sn1	95.1(9)
S4–Sn1–S6	84.7(1)	Sn1–S2–Sn1	88.6(2)
S5–Sn1–S6	123.7(1)	Sn1–S6–Sn2	102.3(2)
		Sn2–S3–Sn2	107.7(2)

TABLE 7
Selected Interatomic Distances (Å) for $Rb_2Sn_4S_9$

Sn1–S2	2.619(6)	Sn2–S8	2.626(6)	Sn3–S1	2.621(6)
Sn1–S5	2.379(6)	Sn2–S10	2.411(6)	Sn3–S10	2.429(6)
Sn1–S7	2.597(6)	Sn2–S14	2.424(6)	Sn3–S11	2.420(6)
Sn1–S9	2.433(6)	Sn2–S1	2.564(5)	Sn3–S16	2.596(6)
Sn1–S13	2.418(6)	Sn2–S6	2.443(7)	Sn3–S15	2.418(6)
Sn4–S2	2.898(6)	Sn5–Sn7	3.821(2)	Sn6–S1	2.856(5)
Sn4–S9	2.405(6)	Sn5–S2	3.405(6)	Sn6–S3	2.417(6)
Sn4–S12	2.412(6)	Sn5–S6	2.422(7)	Sn6–S5	2.528(6)
Sn4–S15	2.513(6)	Sn5–S12	2.391(6)	Sn6–S7	2.351(7)
Sn4–S16	2.375(6)	Sn5–S8	2.347(7)	Sn6–S11	2.402(6)
Sn7–Sn8	3.423(2)	Sn8–S1	3.377(5)		
Sn7–S2	2.552(6)	Sn8–S3	2.375(6)		
Sn7–S4	2.406(6)	Sn8–S14	2.390(6)		
Sn7–S13	2.408(6)	Sn8–S17	2.338(7)		
Sn7–S17	2.628(7)	Sn8–S18	2.429(7)		
Sn7–S18	2.425(7)				
Rb1–S3	3.396(6)	Rb2–S4	3.491(6)		
Rb1–S3	3.544(6)	Rb2–S4	3.767(7)		
Rb1–S5	3.407(6)	Rb2–S6	3.464(7)		
Rb1–S9	4.224(7)	Rb2–S9	3.504(6)		
Rb1–S10	3.334(6)	Rb2–S9	3.790(6)		
Rb1–S10	4.351(6)	Rb2–S10	3.888(6)		
Rb1–S11	3.509(7)	Rb2–S13	3.577(6)		
Rb1–S14	3.692(7)	Rb2–S15	3.362(7)		
Rb1–S16	3.470(6)				
Rb3–S2	3.618(6)	Rb4′–S1	3.622(1)		
Rb3–S5	3.647(6)	Rb4′–S6	4.013(1)		
Rb3–S8	3.297(7)	Rb4′–S7	4.315(1)		
Rb3–S11	3.537(7)	Rb4′–S7	3.804(1)		
Rb3–S14	3.381(7)	Rb4′–S12	3.578(1)		
Rb3–S18	3.701(7)	Rb4′–S13	3.340(1)		
Rb3–S18	3.710(7)	Rb4′–S15	3.606(1)		
		Rb4′–S17	3.359(1)		

lattice modes or from vibrations associated with the alkali cations.

A representative optical transmission spectrum collected from a single crystal of $Cs_2Sn_4S_9$ and converted to absorption data is shown in Fig. 8. Bandgaps were obtained from extrapolation of the data along the absorption edges and found to be 2.66 eV for $Cs_2Sn_4S_9$, 2.65 eV for $Rb_2Sn_4S_9$, and 2.66 eV for $K_2Sn_4S_9$. The presence of optical gaps and the electron-precise nature of these compounds confirms that we are dealing with semiconductors. The transitions responsible for these bandgaps are probably charge transfer in character from the primarily S-based valence bands to the primarily Sn-based conduction bands.

Differential thermal analysis, DTA, was used to characterize $Cs_2Sn_4S_9$, $Rb_2Sn_4S_9$, and $K_2Sn_4S_9$. These layered materials were not ground for use in DTA experiments because they tend to smear into agglomerates rather than pulverize into finely separated particles. $Cs_2Sn_4S_9$ and $Rb_2Sn_4S_9$ samples were heated at a rate of $+10$°C/min to 750°C and cooled at -10°C/min to 200°C and 100°C, respectively, for two consecutive cycles in the DTA. A $K_2Sn_4S_9$ sample was heated at a rate of $+10$°C/min to 700°C and cooled at -10°C/min to 100°C for two consecutive cycles in the DTA. All three compounds exhibited the same melting and recrystallization temperatures during both the first and second heating and cooling cycles, indicating that they melt and recrystallize congruently. A representative plot of the first cycle of the DTA data obtained for $Rb_2Sn_4S_9$ is shown in Fig. 9. $Cs_2Sn_4S_9$ exhibits a melting endotherm at 676°C and a cooling exotherm at 635°C, $Rb_2Sn_4S_9$ exhibits a melting transition at 655°C and recrystallizes at 614°C, and $K_2Sn_4S_9$ melts at 617°C and recrystallizes at 595°C. The X-ray powder diffraction pattern of the DTA residue from $A_2Sn_4S_9$ appeared to be identical to that from the corresponding starting materials.

In summary, the new compounds $Cs_2Sn_4S_9$, and $Rb_2Sn_4S_9$ crystallize in two new related structure types but share the same $[Sn_4S_9]^{2-}$ layer. They were first discovered through the molten polychalcogenide flux synthetic technique and later prepared as microcrystalline products in high yield by direct combination reactions. The Sn/S framework in the $K_2Sn_4S_9$ phase is most likely structurally

TABLE 8
Selected Interatomic Bond Angles (°) for $Rb_2Sn_4S_9$

S2–Sn1–S5	92.81(19)	S1–Sn2–S5	121.00(16)
S2–Sn1–S6	124.09(16)	S1–Sn2–S6	91.90(21)
S2–Sn1–S7	176.07(20)	S1–Sn2–S8	178.36(19)
S2–Sn1–S9	89.35(19)	S1–Sn2–S10	90.07(20)
S2–Sn1–S13	88.03(19)	S1–Sn2–S14	95.66(19)
S5–Sn1–S6	143.05(17)	S6–Sn2–S8	87.15(21)
S5–Sn1–S7	89.07(21)	S6–Sn2–S10	112.66(22)
S5–Sn1–S9	126.23(21)	S6–Sn2–S14	128.97(23)
S5–Sn1–S13	121.24(21)	S8–Sn2–S10	91.53(21)
S7–Sn1–S9	86.76(20)	S8–Sn2–S14	83.91(20)
S7–Sn1–S13	93.95(20)	S10–Sn2–S14	117.70(22)
S9–Sn1–S13	112.52(21)		
S1–Sn3–S3	119.44(16)	S2–Sn4–S4	120.05(14)
S1–Sn3–S10	88.34(19)	S2–Sn4–S9	83.62(18)
S1–Sn3–S11	89.19(19)	S2–Sn4–S12	92.26(18)
S1–Sn3–S15	92.42(20)	S2–Sn4–S15	174.94(20)
S1–Sn3–S16	175.78(18)	S2–Sn4–S16	83.27(18)
S10–Sn3–S11	118.04(21)	S9–Sn4–S12	112.46(21)
S10–Sn3–S15	116.06(21)	S9–Sn4–S15	98.92(21)
S10–Sn3–S16	94.81(20)	S9–Sn4–S16	116.46(22)
S11–Sn3–S15	125.90(22)	S12–Sn4–S15	90.82(20)
S11–Sn3–S16	86.84(19)	S12–Sn4–S16	129.93(20)
S15–Sn3–S16	88.73(20)	S15–Sn4–S16	91.68(21)
S6–Sn5–S8	94.28(22)	S2–Sn7–S4	97.42(19)
S6–Sn5–S12	101.16(22)	S2–Sn7–S13	89.79(19)
S8–Sn5–S12	120.17(20)	S2–Sn7–S17	177.90(21)
S1–Sn6–S3	92.52(18)	S2–Sn7–S18	90.67(20)
S7–Sn6–S11	123.27(22)	S4–Sn7–S13	114.57(23)
S1–Sn6–S5	173.32(19)	S4–Sn7–S17	84.68(21)
S1–Sn6–S7	83.58(20)	S4–Sn7–S18	124.93(23)
S1–Sn6–S11	84.23(18)	S13–Sn7–S17	89.23(21)
S3–Sn6–S5	93.88(20)	S13–Sn7–S18	119.86(22)
S3–Sn6–S7	124.09(21)	S17–Sn7–S18	88.21(22)
S3–Sn6–S11	111.61(20)		
S5–Sn6–S7	91.22(21)		
S5–Sn6–S11	95.20(20)		
S1–Sn8–S3	81.27(17)		
S1–Sn8–S14	77.71(18)		
S1–Sn8–S16	121.49(13)		
S1–Sn8–S17	79.51(20)		
S1–Sn8–S18	174.12(19)		
S3–Sn8–S14	108.76(21)		
S3–Sn8–S17	121.19(23)		
S3–Sn8–S18	103.77(21)		
S14–Sn8–S17	120.23(25)		
S14–Sn8–S18	103.17(22)		
S17–Sn8–S18	95.16(24)		

the same as that in the Rb and Cs analogs. Each $[Sn_4S_9]^{2-}$ layer in these new compounds has a noncentrosymmetric structure which is different from currently known $[Sn_4S_9]^{2-}$ layers (12, 13). Finally, given the substantial disorder of alkali atoms in $Cs_2Sn_4S_9$ and $Rb_2Sn_4S_9$ and their lamellar structure, we suggest that these materials may possess good ion-exchange properties.

TABLE 9
Raman and Far-IR Spectra for $Cs_2Sn_4S_9$ and $Rb_2Sn_4S_9$, and $K_2Sn_4S_9$

Raman spectra	$Cs_2Sn_4S_9$	$Rb_2Sn_4S_9$	$K_2Sn_4S_9$
	166	165	163
	186	186	185
	223	232	232 (w)
	270	268	267
	329	329	331
	344 (sh)	352 (w)	
	366	370	361 (sh)
	383	382 (sh)	376
	470 (w)	452 (w)	–
Far-IR spectra	**$Cs_2Sn_4S_9$**	**$Rb_2Sn_4S_9$**	**$K_2Sn_4S_9$**
	169	170 (w)	172 (sh)
	185	184 (w)	181
	220	226 (w)	219
	280 (sh)	280 (w)	278 (w)
	299	302	303
	329 (sh)	328	329
	345	351	350
	368	368	370
	391	394 (sh)	388 (sh)

Note. (sh) signifies that the absorption peak is on the shoulder of another peak and (w) signifies that the absorption had a weak signal. Data are given in wavenumbers (cm^{-1}).

ACKNOWLEDGMENTS

Financial support from the National Science Foundation DMR-9527347 and from Rockwell International Corporation is gratefully acknowledged. This work made use of the SEM facilities of the Center for Electron Optics, Michigan State University. We thank Jason Hanko for critically reading the manuscript. M.G.K. is an A.P. Sloan Foundation, and a Camille and Henry Dreyfus Teacher Scholar 1993–1998. V.P. thanks the Universite de Nantes, IMN for financial support during his stay at IMN and the Grant Agency of the Czech Republic for Grant 202/1996/0085.

REFERENCES

1. K. Susa and H. Steinfink, *J. Solid State Chem.* **3,** 75 (1971).
2. B. Krebs and W. Schiwy, *Z. Anorg. Allg. Chem.* **393,** 63–71 (1973).
3a. W. Mark, J. C. Lindqvist, J. C. Jumas, and E. Philippot, *Acta Cryst. Sect. B* **30,** 2620 (1974).
3b. W. Schiwy, C. Blutau, Gäthje, and B. Krebs, *Z. Anorg. Allg. Chem.* **412,** 1 (1975).
4a. R. L. Bedard, S. T. Wilson, L. D. Vail, E. M. Bennett, and E. M. Flanigen, "Zeolites: Facts, Figures, Future" (P. A. Jacobs and R. A. van Santen, Eds.), p. 375. Elsevier Science, Amsterdam, 1989.
4b. R. L. Bedard, L. D. Vail, S. T. Wilson, and E. M. Flanigen, U.S. Patent 4,880,761 (1989).
5. J. B. Parise, *Science* **251,** 293 (1991).
6. W. S. Sheldrick and H.-G. Braunbeck, *Z. Naturforsch. B* **45,** 1643 (1990).

7. W. S. Sheldrick and H.-G. Braunbeck, *Z. Anorg. Allg. Chem.* **619,** 1300 (1993).
8. J. B. Parise, Y. Ko, J. Rijssenbeek, D. M. Nellis, K. Tan, and S. Koch, *J. Chem. Soc., Chem. Commun.* 527 (1994).
9. P. Enzel, G. S. Henderson, G. A. Ozin, and R. L. Bedard, *Adv. Mater.* **7,** 166 (1995).
10. W. S. Sheldrick, *Z. Anorg. Allg. Chem.* **562,** 23 (1998).
11. W. S. Sheldrick and B. Z. Schaaf, *Z. Anorg. Allg. Chem.* **620,** 1041 (1994).
12a. P. Enzel, G. S. Henderson, G. A. Ozin, and R. L. Bedard, *Adv. Mater.* **7,** 64 (1995).
12b. T. Jiang, A. J. Lough, G. A. Ozin, and D. Young, *Chem. Mater.* **7,** 245 (1995).
13. Y. Ko, K. Tan, D. M. Nellis, S. Koch, and J. B. Parise, *J. Solid State Chem.* **114,** 506 (1995).
14. J.-H. Liao, C. Varotsis, and M. G. Kanatzidis, *Inorg. Chem.* **32,** 2453 (1993).
15. G. A. Marking and M. G. Kanatzidis, *Chem. Mater.* **7,** 1915 (1995).
16. M. G. Kanatzidis and A. C. Sutorik, *Prog. Inorg. Chem.* **43,** 151 (1995).
17. "CERIUS^2, Version 1.6," Molecular Simulations Inc., Cambridge, England, 1994.
18. "TEXSAN-TEXRAY Structure Analysis Package," Molecular Structure Corp., The Woodlands, TX, 1985.
19. G. M. Sheldrick, in "Crystallographic Computing 3" (G. M. Sheldrick, C. Kruger, and R. Goddard, Eds.) p. 175. Oxford Univ. Press, Oxford, UK, 1985.
20. V. Petricek and M. Dusek, "JANA98," Institute of Physics, Praha, Czech Republic, 1996. [JANA98 is available in http://www-xray.fzu.cz/jana/jana98.html (Praha) or ftp://ftp.unige.ch/pub/soft/crystal/jana/hpageJ98/jana98.html].
21. M. G. Kanatzidis, *Phosphorus, Silicon and Sulfur* **93–94,** 159 (1994).
22. Arguments regarding the counterion effect and the structural trends associated with it are relevant only when the corresponding framework stoichiometry is preserved.
23. E. A. Axtell, J.-H. Liao, Z. Pikramenou, and M. G. Kanatzidis, *Chem. Eur. J.* **2,** 656 (1996).